Available online at www.sciencedirect.com

ScienceDirect

Advances in Space Research 67 (2021) 3478–3488

ADVANCES IN SPACE RESEARCH (a COSPAR publication)

www.elsevier.com/locate/asr

Charge-product control approach to electrostatic leader-follower formations in LEO plasma wakes

Jordan Maxwell *, Hanspeter Schaub

Ann & H.J. Smead Department of Aerospace Engineering Sciences, University of Colorado Boulder, 3775 Discover Dr., UCB 429, Boulder, CO 80303, USA

Received 28 December 2019; received in revised form 22 April 2020; accepted 17 May 2020
Available online 30 May 2020

Abstract

The feasibility of using electrostatic forces to stabilize a close-proximity leader-follower formation is investigated. The leader craft is equipped with a set of affixed spheres whose charge is modulated to hold the charged follower craft along a proscribed trajectory to its nominal leader-relative position. This charge structure and the follower craft are constrained to remain in the plasma wake generated behind all LEO craft because the more-dense ambient plasma outside the wake prevents object charging and electric field propagation. Once the formation is achieved, a controlled electric field is generated by the leader to counter relative accelerations from perturbations like differential drag and solar radiation pressure, holding the follow near its nominal position. Two controllers are derived for the system described, incorporating Coulomb accelerations and linearized gravity and drag accelerations. Simulations are run under unmodeled perturbations and sensor noise for different scenarios, demonstrating the challenges and benefits associated with electrostatic actuation.

Keywords: Formation flying; Electrostatic actuation; Spacecraft control; Plasma wakes

1. Introduction

In recent years, a method called electrostatic actuation has been developed to facilitate on-orbit proximity operations in Geosynchronous Equatorial Orbit (GEO). The technique utilizes induced charge distributions on objects' surfaces to generate Coulomb forces and torques to affect relative position and attitude between nearby craft. This technology has the key benefits of being touchless, using virtually no fuel (Cover et al., 1966; King et al., 2002), and being capable of despinning an object – a capacity that conventional methods lack. (Bennett et al., 2015) Electrostatic actuation is highly precise because relatively large object potentials generate small accelerations. No non-renewable resource is expended when applying the technique unless charging a craft via ionized gas emission.

Electrostatic actuation for spacecraft formation control was first studied in 2002 and was predicted to offer propulsion mass savings of up to 98% compared with conventional thrusters across various scenarios. (King et al., 2002) This discovery motivated a great many investigations of formations controlled using only Coulomb forces (Schaub et al., 2004, 2006; Schaub, 2005; Natarajan and Schaub, 2006; Berryman and Schaub, 2007; Vasavada and Schaub, 2008) or incorporating traditional thrusters to create a hybrid control approach. (Saaj et al., 2010) Once electrostatically controlled formations had been studied in some detail, investigations into Coulomb-force driven on-orbit collision avoidance (Wang and Schaub, 2010), orbit element corrections (Hogan and Schaub, 2013, 2015a), relative attitude control (Schaub and Stevenson, 2013; Bennett et al., 2015; Bennett and

* Corresponding author.
E-mail addresses: jordanmaxwell8@gmail.com (J. Maxwell), hanspeter.schaub@colorado.edu (H. Schaub).

https://doi.org/10.1016/j.asr.2020.05.023
0273-1177/

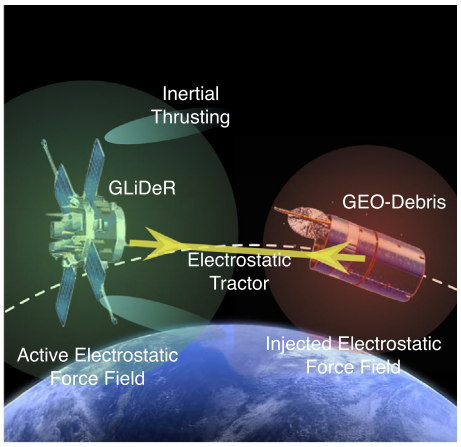

Fig. 1. GLiDeR GEO debris removal concept.

Schaub, 2015; Stevenson and Schaub, 2016), and debris mitigation (Schaub and Moorer, 2014; Schaub and Sternovsky, 2014; Hogan and Schaub, 2015b) (pictured in Fig. 1) demonstrated that electrostatic actuation could facilitate a variety of operations on orbit.

Multiple experimental campaigns have been undertaken to demonstrate the feasibility of electrostatic actuation for relative position and attitude control between nearby objects. A 1-dimensional air bearing track was developed to demonstrate a variety of control scenarios achieved through electrostatic actuation. (Seubert and Schaub, 2010, 2009) Later, a different testbed was developed to demonstrate that the technique could bring an object spinning about a single axis to rest. (Stevenson and Schaub, 2014) While these testbeds provided a baseline for future electrostatic actuation experiments, the presence of atmospheric drag and both testbeds' 1-dimensional nature limit the amount of insight gained for on-orbit applications. While vacuum chamber experiments would provide a more GEO-like environment, the large gravitational force on Earth's surface overwhelms any Coulomb forces that can reasonably be generated.

An ideal environment for demonstrating electrostatic actuation would be that for which these techniques have been developed – GEO – but the substantial cost of putting such a feasibility study into this orbit is likely an insurmountable obstacle. Missions in Low Earth Orbit (LEO) are more affordable and would therefore offer a potential alternative. Until recently, it was assumed that the cold, dense plasma characteristic of much of the ionosphere would prove prohibitive to electrostatic actuation. However, the plasma wakes that form behind objects orbiting in LEO exhibit plasma parameters conducive to the technique.

This paper investigates the application of two control methodologies to two separate formation acquisition scenarios – deployment and rendezvous – within LEO plasma wakes. These operations are of interest because they demonstrate that electrostatic actuation can bring two craft to rest initially traveling at relative speeds on orbit. Fig. 2 depicts the general technique to be applied. A wake-forming leader craft is equipped with a set of isolated conducting spheres which generate a desired electric field — nominally an electrostatic well as shown in Fig. 3. A follower craft is controlled along a chosen reference trajectory to some nominal position $\boldsymbol{\rho}_r$ within the wake.

A significant challenge of applying electrostatic actuation in LEO is the dynamics of the plasma wake. Consider Fig. 2, which shows a variety of charged objects in the wake of the leader craft. These objects will change the potential structure in the wake, leading to changing wake geometry. In the worst case, charging in the wake could result in a potential structure which results in a collapse in which ambient LEO plasma permeates into the wake, precluding the use of electrostatic actuation. This wake collapse behavior is extremely difficult to model, though experimental investigations have been conducted which demonstrate the that the wake volume shrinks when a large negative potential is placed within. (Maxwell and Schaub, 2019) Therefore, control strategies which source low electric potentials on the charged objects are desired.

The attainable potential of an object in the space environment is constrained by the current balance equation. The large electron thermal current and ion ram current prevent objects from attaining large potentials in the ambient ionosphere. Additionally, Debye screening prevents electric fields from propagating an appreciable distance from an object's surface. These two conditions have led researchers to the conclusion that electrostatic actuation is unconformable to such environments. The wake region, however, has much lower density and higher temperatures than ambient (Hastings, 1995), ionospheric plasma so these currents and the screening effect are less substantial.

Wakes form behind orbiting objects in LEO because the orbital velocity is supersonic with respect to the atmospheric neutrals and ionospheric ions. This creates a region antiparallel to the object's velocity that is nearly devoid of these species. (Hastings, 1995) Electrons, which have extremely low mass, move much more rapidly and are therefore able to penetrate into the wake. However, the lack of ions in this region creates a negative space charge which screens out lower-energy electrons, so the electron density is decreased and the temperature increased. Additionally, the geomagnetic field will affect the behavior of the electrons in particular because of their low mass. (Usui et al., 2019) Because the wake always forms in the direction antiparallel to the velocity, the angle between the spacecraft's velocity vector and the local magnetic field must be taken into account. Therefore, the wake's properties will depend on the spacecraft's orbit.

An important feature of the wake is that it contains a nearly pure electron plasma, meaning that the canonical Debye-Hückle theory is inapplicable. An analytic frame work exists which describes screening in a pure electron plasma, demonstrating that the screening affect is asymmetric in potential – positive potentials are screened effectively while negative potentials are not. (Durand de

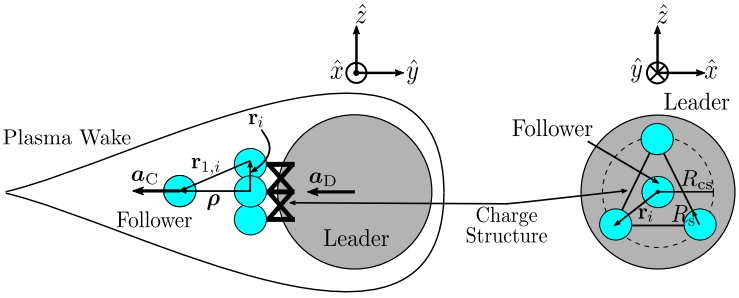

Fig. 2. Off-axis (left) and on-axis (right) views of the LEO electrostatic actuation system. Axes indicate the Hill-Clohessy-Whiltshire (HCW) frame directions.

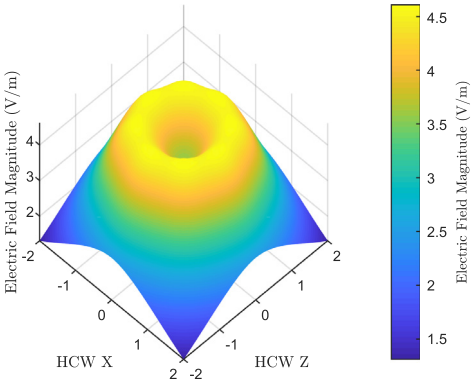

Fig. 3. The electric field 1 m behind the charge structure for a configuration with 8 charged spheres arranged in a circle of radius 1 m.

Gevigney et al., 2011) Indeed, a negatively charged object in an electron plasma creates a localized, evacuated region that exhibits little to no screening. This proves beneficial to electrostatic actuation in that negatively signed electric fields will propagate much farther in the wake and reduce the thermal electron current by thinning out the electron density in that region. This allows for more significant positive voltages on the follower craft and reduced screening.

A substantial body of research supports the development of the proposed technique. References (Martin, 1974; Miyake et al., 2013) numerically model wake structures in LEO-like plasmas for objects of various sizes, geometries, and voltages, while (Svenes and Treim, 2007; Miloch, 2010) use simulation chambers to analyze wake structures behind objects of different sizes, geometries, speeds, and voltages. A variety of missions have been conducted to analyze spacecraft charging and beam structures within LEO, including CHAWS (Davis and Mandell, 1999) and SEPAC (Sasaki et al., 1986), the latter of which showed that objects in the wake can be charged to ~ 5 kV with a ~ 800 W electron gun. Prior work indicates that lower voltages can be sourced to counter LEO perturbations (Maxwell et al., 2018) so lower-wattage guns could likely be flown, resulting in a less substantial impact on the overall spacecraft design.

As discussed in detail previously, applications for electrostatic actuation in GEO have been a focus of much research. However, the constraints introduced by the plasma wake are unique to LEO applications, so significant modifications must be made to the simulation scenarios and control development.

This paper begins with a brief description of the problem to be investigated, following which nonlinear dynamics and control strategies are derived for the system shown in Fig. 2. Finally, results from control simulations are presented and the performance of the controllers are analyzed.

2. Problem statement

Two separate scenarios – deployment and rendezvous – are considered using the electrostatic actuation system shown in Fig. 2. These operations are of interest because they are a necessary part of any electrostatic actuation demonstration and show that the technique can bring to rest a system that is moving at relative-orbital speeds (~ 1 cm/s). Important to note is the assumption throughout this investigation that the plasma wake is a pure vacuum. As discussed previously, the wake does contain plasma and behaves dynamically under electromagnetic perturbations, however the lack of accurate and convenient models precludes incorporation of these effects. In place of precise understanding of the wake behavior, control strategies and system configurations which result in low sourced voltages are sought as these will perturb the wake less.

The two frames used throughout the problem described above are the Earth Centered Inertial (ECI) frame and the Hill (HCW) frame, denoted $\mathcal{N}$ and $\mathcal{H}$, respectively. Note that the HCW frame is also commonly called the Local Vertical, Local Horizontal frame. The formal definitions of the frames are provided below where $\hat{\boldsymbol{n}}_i$ signifies an inertial unit vector, $\hat{\boldsymbol{r}}_{\mathrm{L}}$ is the leader's normalized position relative to the center of the earth, and $\hat{\boldsymbol{h}}_{\mathrm{L}}$ is the direction of the leader's angular momentum vector.

$$\mathcal{N}:\{\hat{\boldsymbol{n}}_1,\hat{\boldsymbol{n}}_2,\hat{\boldsymbol{n}}_3\},\mathcal{H}:\{\hat{\boldsymbol{r}}_{\mathrm{L}},\hat{\boldsymbol{h}}_{\mathrm{L}}\times\hat{\boldsymbol{r}}_{\mathrm{L}},\hat{\boldsymbol{h}}_{\mathrm{L}}\} \tag{1}$$

Throughout this paper, bolded quantities indicate vectors. A left superscript indicates the frame in which a given vector is defined, while the hat notation indicates a unit vector (i.e. ${}^{\mathcal{N}}\hat{\boldsymbol{x}}$ indicates the unit vector of $\boldsymbol{x}$ expressed in the inertial frame). In general, matrices are signified via square brackets, though Direction Cosine Matrices

(DCMs) are identified, for example, by the form $[\mathcal{HN}]$ indicating the mapping of a right multiplied vector from the inertial to the Hill frame.

$$^{\mathcal{H}}\boldsymbol{x} = [\mathcal{HN}]^{\mathcal{N}}\boldsymbol{x}, [\mathcal{HN}] = [^{\mathcal{H}}\hat{\boldsymbol{n}}_1, ^{\mathcal{H}}\hat{\boldsymbol{n}}_2, ^{\mathcal{H}}\hat{\boldsymbol{n}}_3] \tag{2}$$

Finally, a notation for time derivatives as seen by different frames is introduced.

$$\dot{\boldsymbol{x}} = {}^{\mathcal{N}}\frac{\partial \boldsymbol{x}}{\partial t}, \boldsymbol{x}\prime = {}^{\mathcal{H}}\frac{\partial \boldsymbol{x}}{\partial t} \tag{3}$$

Additional notations will be introduced throughout the text, but the definitions above provide a baseline for beginning the analysis.

3. Nonlinear equations of motion

Three perturbations are included in the simplified model used to develop the controllers for the simulation: two-body gravity, orbital drag, and Coulomb forces. The Hill-Clohessy-Whiltshire (HCW) frame is used with the origin at the center of the charge structure attached to the leader. Therefore, the accelerations of the follower relative to the leader are used throughout.

$$^{H}\boldsymbol{\rho} = [\mathcal{HN}]\left({}^{N}\boldsymbol{r}_{\mathrm{F}} - {}^{N}\boldsymbol{r}_{\mathrm{L}}\right) \tag{4}$$

Henceforth, the left superscript on $\boldsymbol{\rho}$ and its derivatives are suppressed. The state of the system is defined $\boldsymbol{X} = [\boldsymbol{\rho}, \dot{\rho}]^T$ and evolves according to the equation

$$\dot{\boldsymbol{X}} = \begin{bmatrix} \dot{\boldsymbol{\rho}} \\ \ddot{\boldsymbol{\rho}}(\boldsymbol{X}, \boldsymbol{Q}) \end{bmatrix} \tag{5}$$

where $\ddot{\boldsymbol{\rho}}$ is a non-linear vector function of the state and charges $\boldsymbol{Q}$ on the follower and charge structure spheres.

3.1. Coulomb acceleration

The Coulomb acceleration of the follower relative to the leader is calculated as the product of the charge on the follower Q_{F} and the electric field of the leader $\boldsymbol{E}_{\mathrm{L}}$ divided by the follower mass m_{F}.

$$\boldsymbol{a}_{\mathrm{C}}(\boldsymbol{X}, \boldsymbol{Q}) = \frac{Q_{\mathrm{F}}\boldsymbol{E}_{\mathrm{L}}(\boldsymbol{X}, \boldsymbol{Q})}{m_{\mathrm{F}}} \tag{6}$$

The proximity of the follower to the charge structure on the leader means that a mutual capacitance exists between the two objects. This effect is described by the relation between the voltage and the charge on a given object.

$$V_i = k_c\frac{Q_i}{R_i} + k_c\sum_{j=1, j\neq i}^{n}\frac{Q_j}{r_{i,j}} \tag{7}$$

Here, $k_{\mathrm{C}} = 8.99 \times 10^9 \mathrm{Nm}^2/\mathrm{C}^2$ is Coulomb's constant, R_i is the radius of the i^{th} sphere, and $r_{i,j}$ is the distance between the i^{th} and j^{th} spheres' centers. Throughout this paper, the subscript 1 refers to the follower and subscripts 2 through n refer to the spheres on the charge structure. The relation above can be rewritten into a single matrix equation.

$$\begin{pmatrix} V_1 \\ V_2 \\ \vdots \\ V_n \end{pmatrix} = k_c \begin{bmatrix} \frac{1}{R_1} & \frac{1}{r_{1,2}} & \cdots & \frac{1}{r_{1,n}} \\ \frac{1}{r_{2,1}} & \frac{1}{R_2} & \cdots & \frac{2}{r_{2,n}} \\ \vdots & \vdots & \ddots & \vdots \\ \frac{1}{r_{n,1}} & \frac{1}{r_{n,2}} & \cdots & \frac{1}{R_n} \end{bmatrix} \begin{pmatrix} Q_1 \\ Q_2 \\ \vdots \\ Q_n \end{pmatrix} \tag{8}$$

Written in a more compact fashion

$$\boldsymbol{V} = [S]\boldsymbol{Q} \tag{9}$$

where $[S]$ is the elastance matrix. (Smythe, 1988) Another expression relating charge to voltage, $\mathbf{Q} = [C]\mathbf{V}$ indicates that the capacitance is the inverse of the elastance matrix.

$$\mathbf{Q} = [S]^{-1}\mathbf{V} \tag{10}$$

With this expression, the unknown quantities is Table 4 — the charge on the follower and electric field of the leader — can be calculated. As shown in Fig. 2, the follower craft is modeled with a single sphere so that its charge is equal to that on sphere 1.

$$Q_{\mathrm{F}} = Q_1 = \boldsymbol{C}_1^T\boldsymbol{V} \tag{11}$$

A more detailed model would require a sum of the spheres modeling the follower craft. The electric field of the leader is the superposition of the individual fields from the charged spheres on the leader craft, which are designated with numbers 2 through n.

$$\boldsymbol{E}_{\mathrm{L}} = \sum_{i=2}^{n}\frac{Q_i}{r_{1,i}^3}\boldsymbol{r}_{1,i} \tag{12}$$

Here, $\boldsymbol{r}_{1,i}$ is a vector pointing from the i^{th} sphere to the follower craft. The collection of charged spheres on the leader create an electrostatic potential well like that shown in Fig. 3 according to this equation. Combining with Eq. (6) yields the acceleration of the follower in terms of only the distance between the follower and each sphere and the charges. Recall from previous discussion that the follower craft is indicated by the numeral 1 to indicate its position within Eq. (8). Substituting the follower charge and leader electric field equations, the Coulomb acceleration on the follower craft is calculated.

$$\boldsymbol{a}_{\mathrm{C}}(\boldsymbol{X}, \boldsymbol{Q}) = \frac{k_{\mathrm{C}}Q_1}{m_{\mathrm{F}}}\sum_{i=2}^{n}\frac{Q_i}{r_{1,i}^3}\boldsymbol{r}_{1,i} \tag{13}$$

3.2. Orbit perturbations

The orbit perturbations in all simulations to follow include nonlinear J_2 gravity, drag, and Solar Radiation Pressure (SRP) accelerations. For each spacecraft, the gravitational acceleration is calculated given the gravitational constant of Earth μ, its oblateness coefficient J_2, its equatorial radius r_{eq}, the position of the spacecraft relative to the center of earth $\boldsymbol{r}$, and the instantaneous angle between the equatorial plane and the spacecraft position vector ϕ.

$$\boldsymbol{a}_{\mathrm{G}} = -\frac{\mu}{r^3}\boldsymbol{r} - \frac{3\mu r_{\mathrm{eq}}}{2r^5}J_2\left[(1-5\sin^2\phi)\boldsymbol{r} + 2r\sin\phi\hat{\boldsymbol{k}}\right] \tag{14}$$

Canonball drag and SRP models are used, as spherical craft are assumed in the scenario. The drag model used is shown below where A is the cross-sectional area, m the mass, C_{D} the drag coefficient, ρ_{atm} the local atmospheric density, and v_{rel} the atmosphere-relative velocity of a given craft.

$$\boldsymbol{a}_{\mathrm{D}} = -\frac{1}{2}\frac{AC_{\mathrm{D}}\rho_{\mathrm{atm}}}{m}v_{\mathrm{rel}}^2\hat{\boldsymbol{v}}_{\mathrm{rel}} \tag{15}$$

The model used for SRP is calculated

$$\boldsymbol{a}_{\mathrm{SRP}} = \frac{\Phi_{\mathrm{S}}C_{\mathrm{R}}A}{m}\frac{AU^2}{u^3}\boldsymbol{u} \tag{16}$$

where Φ_{S} is the solar flux at Earth, C_{R} is the reflectivity coefficient, AU is the astronomical unit, and $\boldsymbol{u}$ is the vector from the sun to a given spacecraft.

3.3. Relative equations of motion

The accelerations defined in Eqs. (13)–(15) pertain to each craft individually. However, the controllers derived in later sections are defined based on the relative dynamics between the leader and follower craft. The follower gravity and drag accelerations relative to the leader are written. Recall that the controller includes only two-body gravity, while the simulation perturbations include the J_2 term.

$$\delta\boldsymbol{a}_{\mathrm{D}} = -\frac{1}{2}\left(\frac{A_{\mathrm{F}}C_{\mathrm{D_F}}\rho_{\mathrm{atm_F}}}{m_{\mathrm{F}}} - \frac{A_{\mathrm{L}}C_{\mathrm{D_L}}\rho_{\mathrm{atm_L}}}{m_{\mathrm{L}}}\right)v_r\boldsymbol{v}_r \tag{17}$$

$$\delta\boldsymbol{a}_{\mathrm{G}} = -\mu\left(\frac{\boldsymbol{r}_{\mathrm{F}}}{r_{\mathrm{F}}^3} - \frac{\boldsymbol{r}_{\mathrm{L}}}{r_{\mathrm{L}}^3}\right) \tag{18}$$

Note above that it is assumed that the atmosphere-relative velocities are identical between the two craft. Given that the differences in area, mass, drag coefficient, and local density dominate the differential drag term for such close-proximity craft, this is a reasonable assumption. A similar assumption that $\boldsymbol{r}_{\mathrm{F}} = \boldsymbol{r}_{\mathrm{L}}$ cannot be made in the gravity case, as differential gravitational accelerations arise only from the difference in these positions.

The relative Coulomb acceleration is written recalling that the Coulomb force on each craft is equal and opposite ($\boldsymbol{F}_{\mathrm{C_F}} = -\boldsymbol{F}_{\mathrm{C_L}}$).

$$\begin{aligned}\delta\boldsymbol{a}_{\mathrm{C}} &= \frac{1}{m_{\mathrm{F}}}\boldsymbol{F}_{\mathrm{C_F}} - \frac{1}{m_{\mathrm{L}}}\boldsymbol{F}_{\mathrm{C_L}} \\ &= k_{\mathrm{C}}\left(\frac{m_{\mathrm{F}}+m_{\mathrm{L}}}{m_{\mathrm{F}}m_{\mathrm{L}}}\right)Q_1\sum_{i=2}^{n}\frac{Q_i}{r_{1,i}^3}\boldsymbol{r}_{1,i}\end{aligned} \tag{19}$$

Finally, the total acceleration of the follower craft relative to the leader is the sum of the Coulomb, gravitational, and drag acceleration differences between the two craft.

$$\ddot{\boldsymbol{\rho}} = \delta\boldsymbol{a}_{\mathrm{C}} + \delta\boldsymbol{a}_{\mathrm{D}} + \delta\boldsymbol{a}_{\mathrm{G}} \tag{20}$$

4. Control development

Prior work has applied voltage as the control variable for electrostatic actuation simulations (Maxwell et al., 2018) as this quantity can be sourced directly unlike charge. It is clear upon inspection of Eq. (10) that the equations of motion described in Eq. (13) are nonlinear in voltage. However, they are linear in the control vector $\boldsymbol{U} = [Q_1Q_2, Q_1Q_3, \ldots, Q_1Q_n]^T$. This charge product control scheme eliminates the presence of the non-linearities which proved the downfall of the voltage control method. (Natarajan and Schaub, 2006).

Applying this control vector, Eq. (13) is rewritten.

$$\delta\boldsymbol{a}_{\mathrm{C}}(\boldsymbol{X},\boldsymbol{U}) = k_{\mathrm{C}}\left(\frac{m_{\mathrm{F}}+m_{\mathrm{L}}}{m_{\mathrm{F}}m_{\mathrm{L}}}\right)[r]\boldsymbol{U} = [B]\boldsymbol{U} \tag{21}$$

The quantity $[r] = \left[\frac{r_{1,2}}{r_{1,2}^3}, \frac{r_{1,3}}{r_{1,3}^3}, \ldots, \frac{r_{1,n}}{r_{1,n}^3}\right]$ is defined to remove the summation and simplify later calculations. With this linear Coulomb acceleration expression, two controllers are derived to control the follower craft along prescribed trajectories in later simulations.

4.1. Linear Quadratic Tracking (LQT)

The first controller applied to the electrostatic actuation problem employs optimal control techniques for a deployment scenario. The limited size of the plasma wake in which electrostatic actuation is possible motivates the implementation of a tracking formulation in which the follower is controlled along a predetermined trajectory from the leader craft to its nominal location. This control methodology was chosen because, in addition to the reference trajectory, the state feedback and control can be directly tuned with gains. Other control formulations — such as the second presented in this paper — exhibit tuning parameters that affect control usage indirectly.

The chosen cost function is that of the classic Linear Quadratic Tracking (LQT) problem, where $\boldsymbol{X}_r$ is the reference trajectory, $[Q]$ is the state feedback gain, $[R]$ the control gain, and τ is the simulation duration.

$$J = \frac{1}{2}\int_{\tau}(\boldsymbol{X}-\boldsymbol{X}_r)^T[Q](\boldsymbol{X}-\boldsymbol{X}_r) + \boldsymbol{U}^T[R]\boldsymbol{U}\mathrm{d}t \tag{22}$$

The optimal control framework applied below could be modified to derive a reference trajectory which minimizes control usage (subject to a selected gain and final state and time) but a prescribed trajectory provides a means of better ensuring that the follower does not leave the limits of the plasma wake. The Hamiltonian of the system is

$$\mathcal{H} = \frac{1}{2}\left[(\boldsymbol{X}-\boldsymbol{X}_r)^T[Q](\boldsymbol{X}-\boldsymbol{X}_r) + \boldsymbol{U}^T[R]\boldsymbol{U}\right] + \lambda^T\dot{\boldsymbol{X}} \tag{23}$$

Applying the necessary conditions yields

$$\dot{\boldsymbol{X}} = \frac{\partial \mathcal{H}}{\partial \lambda} = \dot{\boldsymbol{X}} \tag{24}$$

$$\boldsymbol{0} = \frac{\partial \mathcal{H}}{\partial \boldsymbol{U}} = [R]\boldsymbol{U} + \left[\frac{\partial \dot{\boldsymbol{X}}}{\partial \boldsymbol{U}}\right]\lambda \tag{25}$$

$$\dot{\lambda} = -\frac{\partial \mathcal{H}}{\partial \boldsymbol{X}} = -[Q](\boldsymbol{X} - \boldsymbol{X}_r) - \left[\frac{\partial \dot{\boldsymbol{X}}}{\partial \boldsymbol{X}}\right]\lambda \tag{26}$$

The Jacobian of the dynamics with respect to the control is simple given the linear dynamics demonstrated in Eq. (21).

$$\left[\frac{\partial \dot{\boldsymbol{X}}}{\partial \boldsymbol{U}}\right] = [B] \tag{27}$$

The Jacobian with respect to the states is considered in terms of the block matrices.

$$\left[\frac{\partial \dot{\boldsymbol{X}}}{\partial \boldsymbol{X}}\right] = [A] = \begin{bmatrix} \left[\frac{\partial \dot{\boldsymbol{\rho}}}{\partial \boldsymbol{\rho}}\right] & \left[\frac{\partial \dot{\boldsymbol{\rho}}}{\partial \dot{\boldsymbol{\rho}}}\right] \\ \left[\frac{\partial \ddot{\boldsymbol{\rho}}}{\partial \boldsymbol{\rho}}\right] & \left[\frac{\partial \ddot{\boldsymbol{\rho}}}{\partial \dot{\boldsymbol{\rho}}}\right] \end{bmatrix} = \begin{bmatrix} [0] & [I] \\ \left[\frac{\partial \ddot{\boldsymbol{\rho}}}{\partial \boldsymbol{\rho}}\right] & [0] \end{bmatrix} \tag{28}$$

The simplifications applied in the upper row of Eq. (28) are obvious, but the lower require more description. Only the controller dynamics are included in the Jacobians of the accelerations with respect to the states and rates. None of the accelerations in Eq. (20) depend on the follower velocity.

The primary contribution of this work is the application of the electrostatic actuation system, so the Jacobian of the relative Coulomb acceleration with respect to the follower position is detailed. The quantitiy $\boldsymbol{r}_{1,i} = \boldsymbol{\rho} - \boldsymbol{r}_i$, so its derivative with respect to the follower position is the identity matrix. Consider the derivative of Eq. (19) with respect to the follower position.

$$\left[\frac{\partial \delta \boldsymbol{a}_C}{\partial \boldsymbol{\rho}}\right] = k_C\left(\frac{m_F + m_L}{m_F m_L}\right)\sum_i U_i\left(\boldsymbol{r}^T \frac{\mathrm{d}}{\mathrm{d}\boldsymbol{\rho}}\left(r_{1,i}^{-3}\right) + r_{1,i}^{-3}\frac{\mathrm{d}}{\mathrm{d}\boldsymbol{\rho}}(\boldsymbol{r}_{1,i})\right) \tag{29}$$

The derivative of $r_{1,i}^{-3}$ can be simplified by considering it in terms of a vector inner product.

$$\begin{aligned} \frac{\mathrm{d}}{\mathrm{d}\boldsymbol{\rho}}\left(r_{1,i}^{-3}\right) &= \frac{\mathrm{d}}{\mathrm{d}\boldsymbol{\rho}}\left(\boldsymbol{r}_{1,i}^T\boldsymbol{r}_{1,i}\right)^{-3/2} \\ &= -\frac{3}{2}r_{1,i}^{-5}\left(\boldsymbol{r}_{1,i}^T[I] + \boldsymbol{r}_{1,i}^T[I]\right) = -\frac{3}{r_{1,i}^5}\boldsymbol{r}_{1,i}^T \end{aligned} \tag{30}$$

Substituting this expression into the overall expression for [A] in Eq. (28), the full state dynamics matrix is calculated. Below, the expression $[A_{\mathrm{HCW+Drag}}]$ is calculated as by Harris. (Harris et al., 2018)

$$\left[\frac{\partial \dot{\boldsymbol{X}}}{\partial \boldsymbol{X}}\right] = [A] = \begin{bmatrix} [0] & [I] \\ k_C\sum_{i=1}^{n}\frac{U_i}{r_{1,i}^3}([I] - 3\hat{\boldsymbol{r}}_{1,i}\hat{\boldsymbol{r}}_{1,i}^T) & [0] \end{bmatrix} + [A_{\mathrm{HCW+Drag}}] \tag{31}$$

The equations above are combined to yield the well-known optimal control law for the LQT problem. The remaining derivations are passed over, as the relevant, novel pieces have already been explicated through Eqs. (27) and (31).

$$\boldsymbol{U}_{\mathrm{LQT}}^* = -[R]^{-1}[B]^T([K]\boldsymbol{X} - \boldsymbol{s}) \tag{32}$$

Here, $[K]$ is the numerically precomputed LQT gain matrix and $\boldsymbol{s}$ is related to the reference trajectory. Note that the system is not considered Linear Time-Invariant (LTI), so the Jacobians listed above are recomputed at each timestep.

4.2. Speed-Constrained Kinematic Steering (SCKS)

A control approach similar to that described in (Schaub and Piggott, 2018) is taken in deriving the second controller. Lyapunov's Direct Method is applied to yield a nonlinear control law to actuate the follower craft along a desired trajectory to rendezvous with the leader craft. Recall that the control authority for the electrostatic actuation system shown in Fig. 2 drops off as the relative distance squared. Therefore, a saturating controller is desired so that reasonable voltages are sourced when the craft are far apart. The extreme hazard of collisions on orbit additionally motivates the use of a speed-constrained control law.

A candidate Lyapunov function is proposed.

$$V_1 = \frac{1}{2}\delta\boldsymbol{\rho}^T\delta\boldsymbol{\rho} \tag{33}$$

Here, $\delta\boldsymbol{\rho} = \boldsymbol{\rho} - \boldsymbol{\rho}_r$ is the difference between the current leader-relative position of the follower and the reference trajectory. The derivative of this candidate function is taken below. Since $\dot{V}_1$ must be negative definite for the system to be asymptotically stable, the leader-relative velocity is set equal to an odd function $-\boldsymbol{f}(\delta\boldsymbol{\rho})$.

$$\dot{V}_1 = \delta\boldsymbol{\rho}^T\delta\dot{\boldsymbol{\rho}} = -\delta\boldsymbol{\rho}^T\boldsymbol{f}(\delta\boldsymbol{\rho}) \tag{34}$$

Due to the possibility of collapsing the wake if overly large voltages are sourced, a control that saturates under large position differences is desired. A candidate function with this property is presented. Below, K is a scalar gain and $\delta\dot{\rho}_{\max}$ is the maximum allowed relative follower speed. Note that, as discussed previously, these gain values determine the shape and size of the saturating function $f_i(\delta\boldsymbol{\rho})$, whereas prior gains discussed more directly affected control usage and feedback.

$$f_i(\delta\boldsymbol{\rho}) = \tan^{-1}\left(\delta\rho_i\frac{K\pi}{2\delta\dot{\rho}_{\max}}\right)\frac{2\delta\dot{\rho}_{\max}}{\pi} \tag{35}$$

In order to constrain the leader-relative velocity to adhere to the equation above, an outer control loop must be derived which controls the accelerations. Consider the candidate Lyapunov function below as well as its derivative.

$$V_2 = \frac{1}{2}\Delta\dot{\boldsymbol{\rho}}^T\Delta\dot{\boldsymbol{\rho}} \tag{36}$$

$$\dot{V}_2 = \Delta\dot{\boldsymbol{\rho}}^T\Delta\ddot{\boldsymbol{\rho}} \tag{37}$$

The quantity $\Delta\dot{\boldsymbol{\rho}} = \delta\dot{\boldsymbol{\rho}} - \delta\dot{\boldsymbol{\rho}}^*$ represents the difference between the actual velocity deviation from the reference trajectory and that desired. The combination of the position and velocity control loops is realized by setting $\delta\dot{\boldsymbol{\rho}}^* = \boldsymbol{f}(\delta\boldsymbol{\rho})$. Given this definition, the derivative of $\Delta\dot{\boldsymbol{\rho}}$ is calculated.

$$\Delta\ddot{\boldsymbol{\rho}} = \delta\boldsymbol{a}_{\mathrm{C}} + \delta\boldsymbol{a}_{\mathrm{D}} + \delta\boldsymbol{a}_{\mathrm{G}} - \ddot{\boldsymbol{\rho}}_{\mathrm{r}} + \dot{\boldsymbol{f}}(\delta\boldsymbol{\rho}, \delta\dot{\boldsymbol{\rho}}) \tag{38}$$

The reference trajectory is later defined in the HCW frame for simplicity, so its inertial derivative is computed in terms of its HCW-frame derivatives (denoted by primes rather than dots) and the rotating-frame accelerations.

$$\ddot{\boldsymbol{\rho}}_{\mathrm{r}} = \boldsymbol{\rho}''_{\mathrm{r}} + \dot{\omega}_{\mathcal{H}/\mathcal{N}} \times \boldsymbol{\rho}_{\mathrm{r}} + 2\omega_{\mathcal{H}/\mathcal{N}} \times \boldsymbol{\rho}_{\mathrm{r}}{}' + \omega_{\mathcal{H}/\mathcal{N}} \times \omega_{\mathcal{H}/\mathcal{N}} \times \boldsymbol{\rho}_{\mathrm{r}} \tag{39}$$

Finally, the derivative of the outer-loop saturating control function is presented.

$$\dot{f}_i(\delta\boldsymbol{\rho}, \delta\dot{\boldsymbol{\rho}}) = \frac{K\delta\dot{\rho}_i}{1 + \left(\delta\rho_i \frac{K\pi}{2\delta\dot{\rho}_{\max}}\right)^2} \tag{40}$$

In order to obtain a globally asymptotically stabilizing control, the Lyapunov rate in Eq. (37) is set equal to $-[P]\Delta\dot{\rho}$, where $[P]$ is a matrix gain which determines how strictly the controller holds the spacecraft velocity to that defined in Eq. (35). The resulting control is obtained by using the least-squares inverse of the control effects matrix.

$$\boldsymbol{U}^*_{\mathrm{SCKS}} = -[B]^T([B][B]^T)^{-1}([P](\Delta\dot{\boldsymbol{\rho}}) + \boldsymbol{f}(\delta\boldsymbol{\rho}) + \delta\boldsymbol{a}_{\mathrm{C}} + \delta\boldsymbol{a}_{\mathrm{D}} - \ddot{\boldsymbol{\rho}}_{\mathrm{r}} + \dot{\boldsymbol{f}}(\delta\rho, \delta\dot{\boldsymbol{\rho}})) \tag{41}$$

5. Results & discussion

The LQT and SKCS controllers derived above are applied to deployment and rendezvous simulations, respectively. For both simulations, the leader craft's initial orbit elements are given by $\boldsymbol{r}_{\mathrm{L}} = [7000\mathrm{km}, 0, 0°, 0°, 20°, 10°]^T$ While these two operations are near inverses of one another dynamically, the electrostatic actuation control strategies applied differ dramatically as a result of the electrostatic interactions between the leader and follower. Dominating these effects is the $1/r^2$ Coulomb acceleration dependence which leads to much higher control authority when approaching the leader than when departing. As discussed in the previous section, both control strategies make use of pre-defined reference trajectories. Both simulations consider circular, equatorial 500 km leader orbits. See the spacecraft parameters for both simulations displayed in Table 1. Note that in both simulations, Solar Radiation Pressure (SRP), J_2, and variations in drag are included as unmodeled perturbations.

For both simulations, the controller's knowledge of the follower position and velocity is imperfect. Noise is added to the follower state in the form of a multivariate normal distribution centered on the truth with $\sigma_r = 5$ mm and $\sigma_v = 0.05$ mm as the variances of the positions and velocities, respectively. It is assumed that a variety of sensor information is combined to provide estimates with these noise characteristics.

Table 1
Formation parameters for electrostatic actuation control simulations.

Parameter	Leader	Follower
Number of Charged Spheres	10	1
Charged Sphere Radius (m)	0.25	0.25
Charge Structure Radius (m)	1	N/A
Mass (kg)	1000	1
Drag Coefficient	2.2	2.2
Reflectivity Coefficient	2	2
Cross-Sectional Area (m^2)	3.1415	0.0314

5.1. Reference trajectory design

Trajectories making use of the natural dynamics between the two craft were chosen to reduce the control effort, resulting in the follower traveling to the nominal HCW position ($[0, -1, 0]^T$ m). It is assumed that the initial conditions can be prescribed in both simulations, meaning that some deployment and/or actuation mechanism is available to bring the follower near its nominal position. The HCW formulation specifies a condition on a closed relative orbit. Without developing the formulation required to justify, this condition is that the offset in the HCW-x direction must be null. This is equivalent to saying that the follower and leader craft inertial orbits must have identical semimajor axes. (Schaub and Junkins, 2005) This means that an initial HCW-x velocity on the follower will generate a drift between the two craft which can be taken advantage of.

The HCW State Transition Matrix (STM) is used to map a given position back to the initial state of the follower. While the STM applies linearized gravity to the nonlinear simulation, the extremely close proximity between the leader and follower craft minimizes the resulting error.

$$\boldsymbol{X}_0 = \begin{pmatrix} \boldsymbol{\rho}_0 \\ \dot{\boldsymbol{\rho}}_0 \end{pmatrix} = [\Phi(t_0, t)]\boldsymbol{X}(t) = \begin{bmatrix} [\Phi_{\rho\rho}] & [\Phi_{\rho\dot{\rho}}] \\ [\Phi_{\dot{\rho}\rho}] & [\Phi_{\dot{\rho}\dot{\rho}}] \end{bmatrix} \begin{pmatrix} \boldsymbol{\rho}(t) \\ \dot{\boldsymbol{\rho}}(t) \end{pmatrix} \tag{42}$$

Eq. (42) can be rearranged to solve for the initial velocity given an initial and final position. Expanding Eq. (42) yields two equations.

$$\boldsymbol{\rho}_0 = [\Phi_{\rho\rho}]\boldsymbol{\rho}(t) + [\Phi_{\rho\dot{\rho}}]\dot{\boldsymbol{\rho}}(t) \tag{43}$$

$$\dot{\boldsymbol{\rho}}_0 = [\Phi_{\dot{\rho}\rho}]\boldsymbol{\rho}(t) + [\Phi_{\dot{\rho}\dot{\rho}}]\dot{\boldsymbol{\rho}}(t) \tag{44}$$

Solving the first equation for $\dot{\boldsymbol{\rho}}(t)$ and rearranging gives an expression to calculation $\dot{\boldsymbol{\rho}}_0$ given the initial and final positions. Importantly, the final velocity must remain free, as the other three parameters are fixed.

$$\dot{\boldsymbol{\rho}}_0 = [\Phi_{\dot{\rho}\rho}]\boldsymbol{\rho}(t) + [\Phi_{\dot{\rho}\dot{\rho}}][\Phi_{\rho\dot{\rho}}]^{-1}(\boldsymbol{\rho}_0 - [\Phi_{\rho\rho}]\boldsymbol{\rho}(t)) \tag{45}$$

This method is applied to generate reference trajectories for both of the following simulations. Note that, while better trajectories could be found using more advanced methods, this paper seeks to find robust control laws so this additional effort is considered out of scope.

5.2. Simulation environment definitions

SRP is included as an unmodeled perturbation. Additionally, the controller development assumes a constant drag acceleration for a given orbit radius. In the simulated environment, both drag and SRP vary as they pass in and out of sunlight. Drag is varied sinusoidally by $\pm 30\%$ to roughly reflect density changes between sun and eclipse (Bruinsma and Forbes, 2008), while SRP is cut completely in shade. These simplified models are described in greater detail in Table 2 where ν is the true anomaly.

5.3. Simulation 1: Deployment scenario applying LQT controller

The first simulation applies the control law in Eq. (32) to the deployment scenario so that the initial follower positions is $\boldsymbol{\rho}_0 = [0, 0, 0]^T$ m. The initial velocity calculated using Eq. (45) and used to generate the reference trajectory is $\dot{\boldsymbol{\rho}}_0 = [0.270, 0, 0]^T$ m/s. The velocity was chosen such that the nominal position is achieved in half an orbit period. As mentioned previously, the final velocity must remain free to solve Eq. (42) for $\dot{\boldsymbol{\rho}}_0$, resulting in a non-zero velocity when the follower reaches the nominal position. Rather than immediately demand that the control cease all motion in the HCW-x direction — which would demand a great amount of control — the trajectory is altered to exponentially decrease the HCW-x velocity throughout another 0.25 orbits.

The matrix gains in Eq. (32) are replaced with scalars for this simulation and displayed in Table 3. Note that R is large because the charge product control vector magnitude is extremely small.

Fig. 4 shows the deviation between the follower's HCW position and velocity and the nominal throughout the simulation. Note that the follower tends to oscillate about the nominal state rather than settling to it. This is due in part to the unmodeled drag and SRP varitations, but also because the gains in Table 3 were not selected to critically damp the system, but rather to balance control usage with an acceptable deviation from the nominal state. Note that, with the selected gains, the nominal positions is held within roughly ± 10 cm.

Table 2
Simplified drag and SRP models.

Drag	SRP
$\rho_{\text{atm}} = \rho_{\text{atm},0}(1 + 0.3\sin\nu)$	$C_{\text{R}} = \begin{cases} C_{\text{R}} & 0 \leqslant \nu < \pi \\ 0 & \pi \leqslant \nu < 2\pi \end{cases}$

Table 3
Gains used in simulation 1.

Parameter	Value
R	2.5×10^{26} C^{-4}
Q	10 m$^{[-2]}$

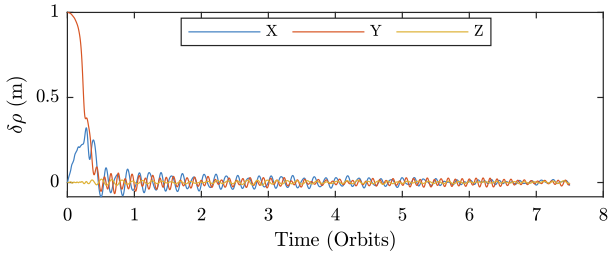

(a) Deviation of HCW position

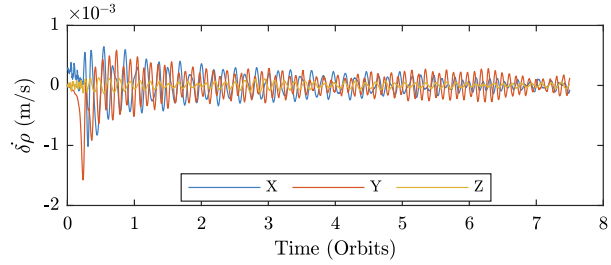

(b) Deviation of HCW velocity

Fig. 4. Deviation of HCW position and velocity relative to nominal for simulation 1.

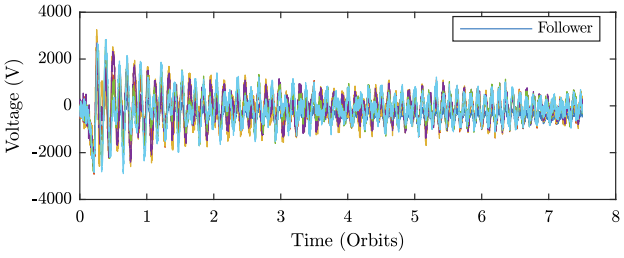

Fig. 5. Control voltage For simulation 1. Only the Follower's line is called out in the legend because the individual behavior of each of the charge structure's spheres is of no interest.

The effects of the added noise is clearly seen in Fig. 5. Interestingly, while the voltage signals certainly exhibit some noisey characteristics, the overall magnitude of the voltages are not increased compared to simulations (not shown) in which perfect knowledge of the follower state is assumed. The voltages sourced by the controller are initially bounded within ± 3000 V, though decay slightly in time. While the voltage limit for wake collapse is highly specific to a given system, generally speaking this voltage is large for LEO applications in which the relative kinetic energy between a craft the ionospheric ions is roughly 10 eV — several orders of magnitude lower than the electrostatic energy between an ion and the craft in this simulation.

The structure of Fig. 5 consists of a period in which the controller sources low potentials followed by a significant step increase as the nominal position is realized. This results from the fact that the reference follower velocity does not go to zero as the reference follwer position does. Therefore, a more carefully designed reference trajectory — in which natural dynamics are leveraged, but the relative position and velocity go to zero together — may reduce the overall control usage for the LQT controller.

Finally, the acceleration magnitudes for simulation 1 are shown in Fig. 6. Note that these are the true, nonlinear accelerations applied in the simulation, not the linearized and abbreviated dynamics included in the controller derivation. The magnitude of the follower Coulomb acceleration is significantly higher than just the drag and SRP perturbations can account for. This is because the controller is also correcting on the differences in the two-body plus J2 accelerations.

5.4. Simulation 2: Rendezvous scenario applying SCKS controller

The second simulation considers a scenario in which the two craft approach in the along-track (HCW-y) direction. Electrostatic actuation is used to place the follower at the nominal HCW state. It is assumed that the follower remains within the plasma wake at all times. The initial conditions are chosen with Eq. (45) to place the follower at the nominal position after a quarter of an orbit. It is important to note that, while the initial conditions are chosen using the HCW STM, the control feeds back on the offset from the nominal state.

The gains in Eq. (41) are displayed in Table 4. The initial HCW state of the follower — which would arrive at the off-nominal position after a quarter period given only HCW dynamics — is [-0.4000 m, −1.3425 m, 0 m, 0.0003 m/s, 0.0006 m/s, 0 m/s]^T.

Table 4
Gains used in simulation 2.

Parameter	Value
K	0.001 1/s
P	0.05 1/s
$\delta\dot{\rho}_{\max}$	0.001 m/s

The difference between the follower state and the nominal for simulation 2 is displayed in Fig. 7. Notice the noise is especially noticeable in the velocity picture in Fig. 4(b) as the enforced limit on $\delta\dot{\rho}_{\max}$ means that the velocity remains near the noise floor. Overall, the settling behavior of simulation 2 is far superior to the behavior for simulation 1 shown in Fig. 4. Indeed, the follower state remains very near the nominal once achieved, with small deviations resulting from unmodeled perturbations.

Note that the system does not settle to the nominal position in a quarter period, even though the initial conditions were intended to place the follower very near that position after that amount of time. This is because the gains and saturated position control are set such that reasonable voltages are sourced. These voltages are displayed in Fig. 8.

An interesting difference between the simulations is the affect of adding noise. Though the same variances were used for both simulations, the SCKS controller does not handle the noise well, as seen in Fig. 8. Simulations assuming perfect knowledge of the follower craft for simulation 2 (not pictured) sourced lower voltages, especially later in the simulation. This behavior can be understood via

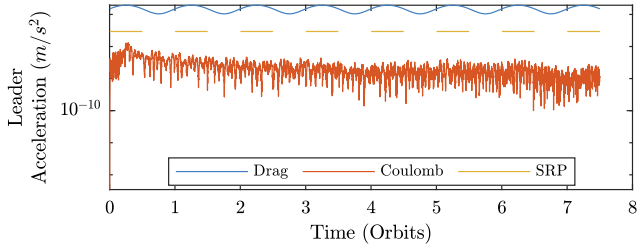

(a) Leader accelerations

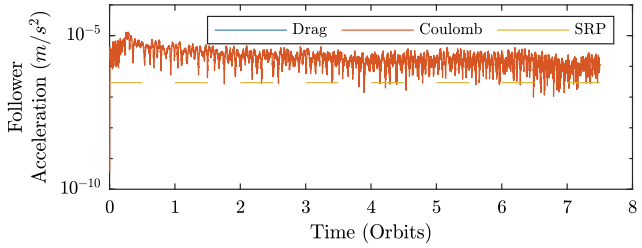

(b) Follower accelerations

Fig. 6. Accelerations for simulation 1.

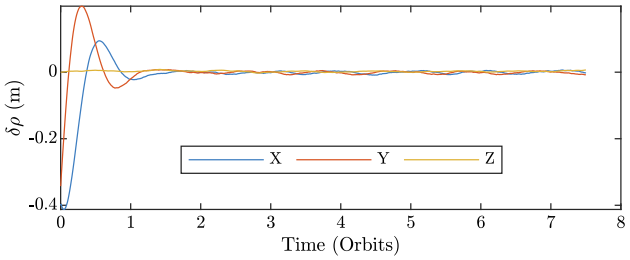

(a) Deviation of HCW position

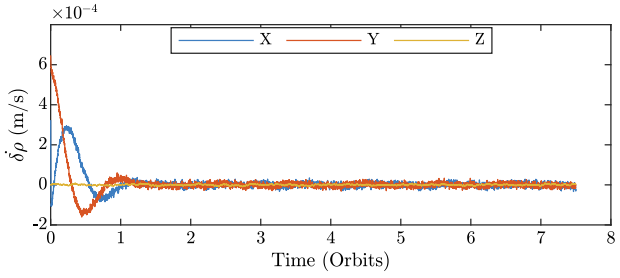

(b) Deviation of HCW velocity

Fig. 7. Deviation of HCW position and velocity relative to nominal for simulation 2.

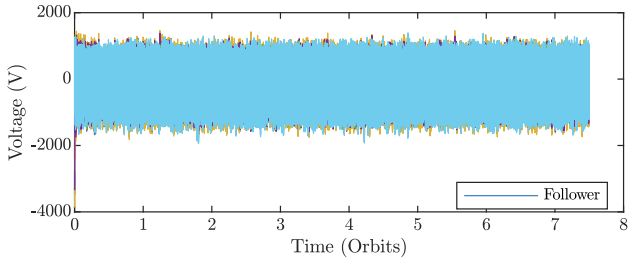

Fig. 8. Control voltages for simulation 2. Only the Follower's line is called out in the legend because the individual behavior of each of the charge structure's spheres is of no interest.

comparison with the LQT controller used in simulation 1. For this first controller, the affect of noise is diminished by the selection of a small state-feedback gain because the small position corruptions resulting from system noise do not generate a significant cost. The SCKS controller on the other hand has gains that allow one to shape the saturating function, but none that directly apply to control usage or state feedback.

While the addition of noise significantly impacts the SCKS controller, note that lower voltages are sourced overall relative to simulation 1. While the deployment versus rendezvous scenarios make one-to-one comparison impossible, it appears that the saturating controller has significant benefits.

The accelerations for simulation 2 are shown in Fig. 9. As with the voltages plotted in Fig. 8, the Coulomb accelerations are extremely noisey, but are of roughly the same magnitude as those in Fig. 6.

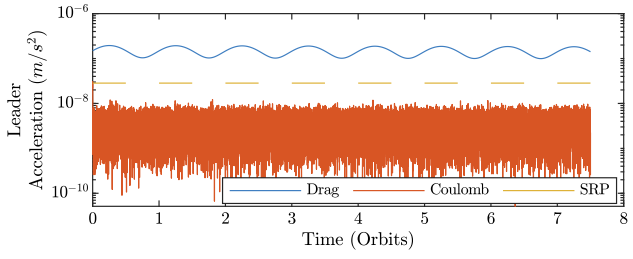

(a) Leader accelerations

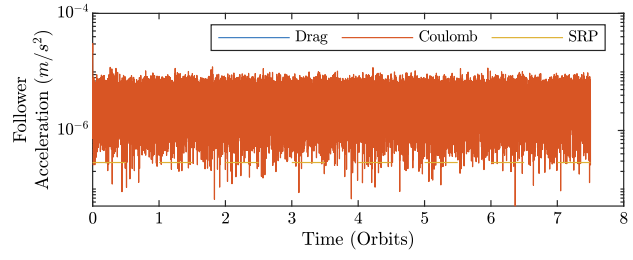

(b) Follower accelerations

Fig. 9. Accelerations for simulation 2.

6. Conclusion

An electrostatic actuation system is presented to control close-proximity leader-follower formations in LEO plasma wakes. Nonlinear dynamics are developed and two control approaches are derived to apply to two separate scenarios. Finally, results are presented which demonstrate the effectiveness of each controller on its respective scenario.

The LQT controller brings the follower to oscillate around the nominal state for many orbits after deployment. This results from gains selected to balance the state deviation and control usage. Large voltages are sourced, but the addition of noise does not compromise the overall performance of the controller due to a state feedback gain chosen to be small.

The rendezvous scenario is achieved using the SCKS controller. The settling behavior and overall control usage is favorable, but the addition of noisey follower state measurements significantly increases control usage. The success of these two techniques in bringing the system — initially with leader and follower moving relative to each-other at ~cm/s velocities — to its nominal configuration indicates that a LEO mission could serve as a proof-of-concept for electrostatic actuation techniques. The addition of noise on the follower positions serves to substantially increase the voltages sourced by the controller. This could prove challenging for a scenario in which the follower craft is of similar dimension to the plasma wake — such that potentials on the follower craft are very near the boundary between the wake the ambient plasma. Other scenarios considering, per se, a cubesat in the wake of the International Space Station may handle this better, as potentials can drop off spatially between the follower craft and the wake boundary.

Acknowledgements

This work was partially supported by the Research and Innovation Seed Grant at the University of Colorado Boulder.

References

Bennett, T., Schaub, H., 2015. Touchless electrostatic three-dimensional detumbling of large axi-symmetric debris. J. Astronaut. Sci. 62 (3), 233–253.

Bennett, T., Stevenson, D., Hogan, E., McManus, L., Schaub, H., 2015. Prospects and challenges of touchless debris despinning using electrostatics. Adv. Space Res. 56 (3), 557–568.

Berryman, J., Schaub, H., 2007. Analytical charge analysis for 2- and 3-craft coulomb formations. AIAA J. Guid. Control Dyn. 30 (6), 1701–1710.

Bruinsma, S.L., Forbes, J.M., 2008. Medium-to large-scale density variability as observed by champ. Space Weather 6 (8).

Cover, J.H., Knauer, W., Maurer, H.A., 1966. Lightweight reflecting structures utilizing electrostatic inflation. US Patent 3,546,706.

Davis, V., Mandell, M., 1999. High-voltage interactions in plasma wakes: simulation and flight measurements from the Charge Hazards and

Wake Studies (CHAWS) experiment. J. Geophys. Res. 104 (A6), 12445–12459.
Durand de Gevigney, B., Sunn Pedersen, T., Boozer, A.H., 2011. Debye screening and injection of positrons across the magnetic surfaces of a pure electron plasma in a stellarator. Phys. Plasmas 18 (1), 013508.
Harris, A., Petersen, C.D., Schaub, H., 2018. Linear coupled attitude-orbit control through aerodynamic forces. In: Space Flight Mechanics Meeting, Kissimmee, Florida.
Hastings, D.E., 1995. A review of plasma interactions with spacecraft in low Earth orbit. J. Geophys. Res. 100 (A8), 14457–14483.
Hogan, E., Schaub, H., 2013. Relative motion control for two-spacecraft electrostatic orbit corrections. AIAA J. Guid. Control Dyn. 36 (1), 240–249.
Hogan, E., Schaub, H., 2015a. General high-altitude orbit corrections using electrostatic tugging with charge control. AIAA J. Guid. Control Dyn.. 38 (4), 699–705.
Hogan, E.A., Schaub, H., 2015b. Impacts of tug and debris sizes on electrostatic tractor charging performance. Adv. Space Res. 55 (2), 630–638.
King, L.B., Parker, G.G., Deshmukh, S., Chong, J.-H., 2002. Spacecraft formation-flying using inter-vehicle coulomb forces. NIAC Phase I Final Report.
Martin, A.R., 1974. Numerical Solutions to the problem of charged particle flow around an Ionospheric Spacecraft 22 (d), 121–141.
Maxwell, J., Harris, A., Schaub, H., Oct. 1–5 2018. Balancing differential drag with coulomb repulsion in low earth orbit plasma wakes. In: International Astronautical Congress. Bremen, Germany, paper No. C1,6,2, x45169.
Maxwell, J., Schaub, H., 2019. Low earth orbit plasma wake shaping and applications to on-orbit proximity operations. IEEE Trans. Plasma Sci.
Miloch, W.J., 2010. Wake effects and Mach cones behind objects. Plasma Phys. Controlled Fusion 52 (12), 124004, http://stacks.iop.org/0741-3335/52/i=12/a=124004?key=crossref.3c3a6fd90a2da50430e0ec11b243262b.
Miyake, Y., Cully, C.M., Usui, H., Nakashima, H., 2013. Plasma particle simulations of wake formation behind a spacecraft with thin wire booms. J. Geophys. Res.: Space Phys. 118 (9), 5681–5694.
Natarajan, A., Schaub, H., 2006. Linear dynamics and stability analysis of a coulomb tether formation. J. Guid. Control Dyn. 29 (4), 831–839.
Saaj, C., Lappas, V., Schaub, H., Izzo, D., 2010. Hybrid propulsion system for formation flying using electrostatic forces. Aerosp. Sci. Technol. 14 (5), 348–355.
Sasaki, S., Kawashima, N., Kuriki, K., Yanagisawa, M., Obayashi, T., 1986. Vehicle charging observed in SEPAC Spacelab-1 experiment. J. Spacecraft Rock. 23 (2), 194–199.
Schaub, H., 2005. Stabilization of satellite motion relative to a coulomb spacecraft formation. J. Guid. Control Dyn. 28 (6), 1231–1239.
Schaub, H., Hall, C., Berryman, J., 2006. Necessary conditions for circularly-restricted static coulomb formations. J. Astronaut. Sci. 54 (3–4), 525–541.
Schaub, H., Junkins, J.L., 2005. Analytical mechanics of space systems. Am. Inst. Aeronaut. Astronaut.
Schaub, H., Moorer, D.F., 2014. Geosynchronous large debris reorbiter: challenges and prospects. J. Astronaut. Sci. 59 (1–2), 161–176.
Schaub, H., Parker, G.G., King, L.B., 2004. Challenges and prospect of coulomb formations. J. Astronaut. Sci. 52 (1–2), 169–193.
Schaub, H., Piggott, S., 2018. Speed-constrained three-axes attitude control using kinematic steering. Acta Astronaut. 174, 1–8.
Schaub, H., Sternovsky, Z., 2014. Active space debris charging for contactless electrostatic disposal maneuvers. Adv. Space Res. 43 (1), 110–118.
Schaub, H., Stevenson, D., 2013. Prospects of relative attitude control using coulomb actuation. J. Astronaut. Sci. 60 (3), 258–277.
Seubert, C.R., Schaub, H., 2009. One-dimensional testbed for coulomb controlled spacecraft. In: AAS/AIAA Spaceflight Mechanics Meeting. Savannah, GA, pp. 09–015.
Seubert, C.R., Schaub, H., 2010. Closed-loop one-dimensional charged relative motion experiments simululating constrained orbital motion. AIAA J. Guid. Control Dyn. 33 (6), 1856–1865.
Smythe, W.B., 1988. Static and dynamic electricity.
Stevenson, D., Schaub, H., 2014. Terrestrial testbed for remote coulomb spacecraft rotation control. Int. J. Space Sci. Eng. 2 (1), 96–112.
Stevenson, D., Schaub, H., 2016. Electrostatic spacecraft rate and attitude control – experimental results and performance considerations. Acta Astronaut. 119, 22–33.
Svenes, K.R., Treim, J., 2007. Laboratory simulation of vehicle-plasma interaction in low Earth orbit 42 (1).
Usui, H., Miyake, Y., Miloch, W.J., Ito, K., 2019. Numerical study of plasma depletion region in a satellite wake. IEEE Trans. Plasma Sci.
Vasavada, H., Schaub, H., 2008. Analytic solutions for equal mass four-craft static coulomb formation. J. Astronaut. Sci. 56 (1), 7–40.
Wang, S., Schaub, H., 2010. Electrostatic spacecraft collision avoidance using piece-wise constant charges. AIAA J. Guid. Control Dyn. 33 (2), 510–520.